Structure evolution in poly(ethylene terephthalate) (PET) - Multi-walled carbon nanotube (MWCNT) composite films during *in-situ* uniaxial deformation

Accepted Manuscript

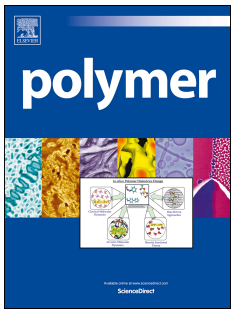

Structure evolution in polyethylene terephthalate (PET) - multi-walled carbon nanotube (MWCNT) composite films during *in-situ* uniaxial deformation

Ellen L. Heeley, Darren J. Hughes, Eleanor Crabb, Matthew Kershaw, Olga Shebanova, Sandy Leung, Tony McNally

PII: S0032-3861(16)30217-8

DOI: 10.1016/j.polymer.2016.03.071

Reference: JPOL 18563

To appear in: *Polymer*

Received Date: 20 January 2016

Revised Date: 18 March 2016

Accepted Date: 22 March 2016

Please cite this article as: Heeley EL, Hughes DJ, Crabb E, Kershaw M, Shebanova O, Leung S, McNally T, Structure evolution in polyethylene terephthalate (PET) - multi-walled carbon nanotube (MWCNT) composite films during *in-situ* uniaxial deformation, *Polymer* (2016), doi: 10.1016/j.polymer.2016.03.071.

Graphical abstract.

Structure evolution in polyethylene terephthalate (PET) - multi-walled carbon nanotube (MWCNT) composite films during *in-situ* uniaxial deformation.

Ellen L. Heeley, Darren J. Hughes, Eleanor Crabb, Matthew Kershaw, Olga Shebanova, Sandy Leung and Tony McNally.

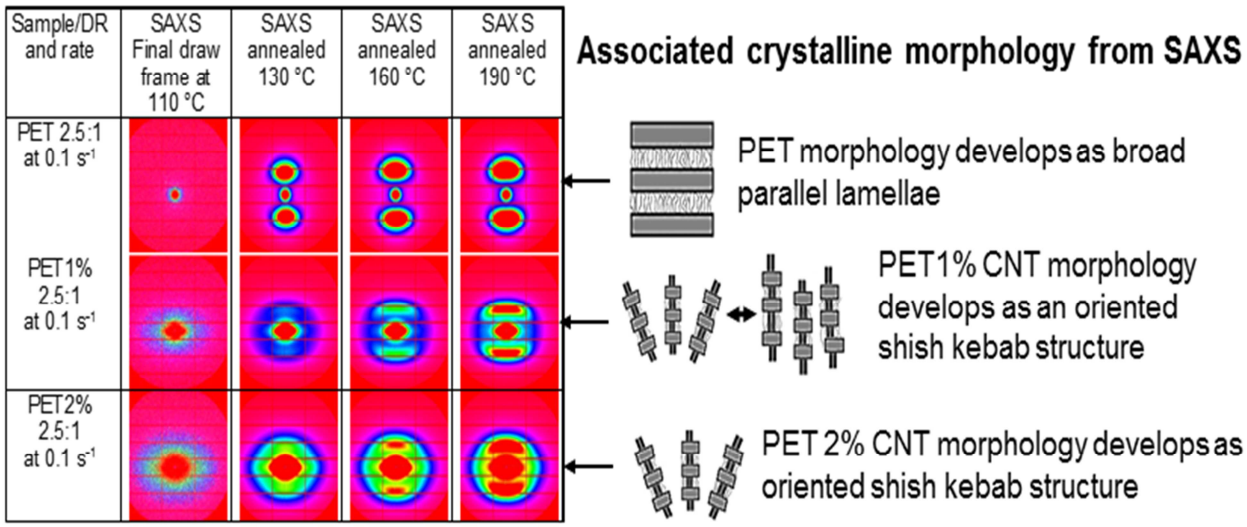

Structure evolution in poly(ethylene terephthalate) (PET) - multi-walled carbon nanotube (MWCNT) composite films during *in-situ* uniaxial deformation.

Ellen L. Heeley,[†*] Darren J. Hughes, [‡] Eleanor Crabb,[†] Matthew Kershaw, [†] Olga Shebanova,[§] Sandy Leung[¥] and Tony McNally[¥]*

[†]Department of Life, Health and Chemical Sciences, Open University, Walton Hall, Milton Keynes, MK7 6AA, UK.

[¥] International Institute for Nanocomposites Manufacturing (IINM), [‡]WMG, University of Warwick, Coventry, CV4 7AL, UK.

[§]Diamond Light Source, Harwell Science and Innovation Campus, Didcot, Oxfordshire, OX11 0DE.

*Corresponding author: E.L. Heeley; Ellen.Heeley@open.ac.uk; +44(0)1908 655194.

Keywords: polymer multi-walled carbon nanotube composites; Small- and Wide-Angle X-Ray Scattering (SAXS/WAXS); crystalline morphology evolution, nucleating agents.

ABSTRACT

Combined small- and wide-angle X-ray scattering (SAXS/WAXS), mechanical and thermal techniques have been used to follow the morphology evolution in a series of poly(ethylene terephthalate) (PET) multiwall carbon nanotube (MWCNT) composite films during quasi solid-state uniaxial deformation at low strain rates. Uniaxially deformed PET-MWCNT films displayed improved mechanical properties compared with unfilled PET films. SAXS/WAXS data revealed a well oriented lamellar structure for unfilled PET films. In contrast, the PET-MWCNT composites revealed a nanohybrid shish-kebab (NHSK) morphology, with reduced

orientation and crystallinity. Mechanistically, this morphology development is attributed to the MWCNTs acting as shish for the epitaxial growth of PET crystallites. Furthermore, nucleation and crystal growth occurs in the PET matrix, but MWCNTs ultimately inhibit crystallite development and hinder a final lamellar structure developing. The results show unequivocally the role MWCNTs play as nanofillers, in the morphology development, thermal and mechanical properties in composite polymer films.

1. INTRODUCTION

Multi-walled and single-walled carbon nanotubes (MWCNTs/SWCNTs or CNTs) continue to be of particular interest in academia and to industry as potential nanoparticulate functional fillers for polymers. It is well known that CNTs possess exceptional electrical, mechanical and thermal properties which can be beneficial in enhancing the physical properties of a polymer when blended into the matrix [1-3]. Indeed, there have been numerous books and reviews published detailing the relative improvements in stiffness, strength, toughness, electrical and thermal conductivity of polymers on the addition of CNTs [3-10]. The physical properties of polymer-CNT composites are governed both by the blending procedure during melt mixing and secondary processing such as moulding, fibre spinning and solid-state film deformation. The CNT dispersal and distribution affects the evolution of micro- and macro-morphology of the host polymer, which ultimately influences its physical and mechanical properties. Furthermore, understanding the evolution of polymer morphology during processing with respect to the influence of CNTs as well as correlating this with mechanical and electrical properties, is of great importance in advancing the applications of polymer nanocomposites.

Here, we focus on a commercially and industrially important polyester; poly(ethylene terephthalate) (PET), which is widely used in many applications such as fibers, films, bottles,

packaging, textiles, automotive parts and engineering components in electronics. The PET homopolymer was physically blended with low loadings of MWCNTs by weight (wt%), with the intention of improving the polymers electrical and mechanical properties. The development of these PET-CNT composite materials could potentially lead to further industrial applications being realized; e.g. in fuel cells and bipolar plates. Recently, Mayoral [11] and McCrossan [12], reported on the structural morphology, electrical and mechanical properties of composites of PET and MWCNTs. The mechanical properties (stiffness, strength and toughness) were vastly modified on addition MWCNTs into the PET matrix: the PET-MWCNT composites showed an enhancement in Young's modulus of 79% and electrical conductivity by 14 orders of magnitude, compared to neat PET.

It is known that the addition of CNTs to PET not only improves the polymers mechanical and electrical properties [10], but also increases the rate of crystallization by acting as a nucleating agent. This is observed during thermal analysis as an increase in the crystallization temperature of the polymer, although, there is often no increase in melting temperature or change in glass transition temperature [11,13-17]. Following the structure evolution in polymer-CNT composites during processing is not straightforward and requires techniques that allow time-resolved data acquisition ranging from less than a second to several minutes depending on the processing conditions. The isothermal crystallization of PET-CNT composites is often monitored using thermal, infrared and X-ray techniques which probe the crystallization kinetics, crystallinity, orientation/chain conformation and confinement of the host polymer [13-15,18-24]. These studies generally investigate the post-processed material either as melt-spun fibres or cast films and hence, do not give a comprehensive understanding of the morphology evolution during

actual processing, i.e. what is the origin of the morphology which develops in the polymer and how does this relate to the role of CNTs in the composites final macro and microstructure.

Recently, Laird [25] presented a perspective on the structure and morphology of polymer-MWCNT composites, in particular CNT–induced polymer crystallization under isothermal and flow conditions. A nanohybrid shish-kebab structure (NHSK) was argued to arise during the solution crystallization of polyethylene (PE) and MWCNTs. It was revealed that the MWCNTs act as heterogeneous nucleation sites; the PE chains wrap around the MWCNTs (which act as the shish) and crystallize outwards epitaxially perpendicular to the MWCNT as the kebabs.[26.27] Likewise, Patil [28] reported that during the flow-induced crystallization (under melt-shear conditions) of PE-SWCNT composites, high shear rates were required to form a NHSK structure in the neat PE. However, a NHSK structure was formed in the composites under low shear conditions where they concluded that the CNTs have a clear role in polymer chain orientation and hence an oriented shish-kebab structure. Also, Liu [29] and Chen [30] described the morphology development in isotactic polypropylene (iPP)-MWCNT composites when injection molded or under melt-shear flow respectively. In each case, using small-angle X-ray scattering (SAXS), the authors suggest that the iPP chains crystallize perpendicularly outwards from the CNTs forming either a lamellar morphology under isotheral conditions, or a mixture of oriented shish-kebab and lamellar morphologies under flow conditions. Wurm [31] investigated the crystallization of poly(ε-caprolactone)(PCL)/MWCNT composite films using combined small- and wide-angle scattering (SAXS/WAXS) and thermal techniques. The authors proposed three scenarios for the crystallization process of PCL-MWCNT composites; (i) nucleation and hence crystallite growth only from the CNT surface, (ii) nucleation in both the polymer matrix and at the CNT surface, (iii) nucleation in the polymer matrix only.

These studies give an insight into the complexity of CNT induced morphology development of polyolefins during isothermal or melt-flow conditions. Yet, with respect to PET-CNT composite films, few studies have investigated the *in-situ* morphology evolution during quasi-solid-state or solid-state deformation, where most typically studies focus on melt-spun fibres after processing. Vad [21] detailed the structure evolution and mechanical properties of high speed melt-spun PET-MWCNT fibres. It was argued that there is a critical draw ratio (DR) for the fibres which induce CNT orientation parallel to the draw direction. Below, this critical DR the CNTs were aligned perpendicular to the draw direction. However, little detailed information of the macro-morphology, whether a NHSK or lamellar structure was presented for the fibres. Anand [20] drew melt-compounded composites of PET and SWCNTs where wide-angle X-ray scattering (WAXS) experiments revealed an oriented PET crystalline structure. They concluded that the CNTs induced the crystallization of PET chains along the CNT axis. Recently, Hur [22] described the morphology and mechanical properties of both PET-MWCNT melt-spun fibres and subsequent photo-thermally drawn fibres. Interestingly, WAXS data showed that at high draw ratios, only the photo-thermally drawn fibres showed an oriented PET crystalline structure. Mayoral [11] confirmed the formation of different crystal polymorphs when composites of PET and MWCNTs in extruded sheet form were uniaxial and biaxial deformed.

It should be noted that the aforementioned studies focused on the application of medium to very high strain rates, which can effectively orient both the CNTs and polymer chains in the fibres/sheets. From these examples, WAXS has been used to show a final oriented PET crystalline micro-structure developed in the PET-MWCNT composites. However, the WAXS technique is limited in its ability to investigate the nature of the macro-structure that evolves during processing in these composites as it probes only the crystalline lattice. To address this

lack of knowledge of the wider morphology evolution, here we present detailed qualitative and quantitative analyses of the real-time micro-macro-structure evolution *in-situ* during solid-state uniaxial deformation of PET-MWCNT composite films using combined SAXS/WAXS techniques. The SAXS technique reveals information pertaining to the long-range packing of the PET-MWCNT composite films, allowing estimation of both the morphology and crystallite dimensions. In this study a purpose-built temperature-controlled polymer film stretching instrument, has been employed to allow time-resolved SAXS and load-displacement data to be obtained during uniaxial deformation (and subsequent annealing) of extruded PET-MWCNT composite films.

The combined use of SAXS, WAXS, mechanical and thermal techniques allows an in-depth insight into the morphological evolution during low strain rate deformation of PET-MWCNT composite films for the first time. The results show unequivocally the role the MWCNTs play in the crystallinity, orientation and morphology development in the polymer composites and how this is correlated to the mechanical and thermal properties they display.

2 EXPERIMENTAL SECTION

2.1 Materials, composite preparation and thermal characterization.

Commercial grade poly(ethylene terephthalate), Polyclear F019 (IV 0.895 dl/g) was supplied by Invista Resins & Fibers Gmbh. A 10 wt% master-batch composite blend of PET-MWCNT was provided by Nanocyl SA, Belgium. The MWCNTs (NC 7000) had an average diameter and length of 9.5 nm and 1.5 μm respectively. From the dilution method used, blends of PET and MWCNTs at loadings of 1 wt% and 2 wt% were cast extruded into sheets 100 mm wide and 1 mm thick. Full details of composite preparation, dilution, and extrusion are given in detail

elsewhere [11]. Each composite is denoted with respect to its MWCNT loading: PET1% and PET2%. Table 1, lists the glass transition temperature (T_g), melting temperature (T_m), crystallization temperature (T_c) and crystallinity (X_c) of the PET-CNT cast composite materials [11]. The dispersion and distribution of the MWCNTs in the polymer matrix were investigated using various microscopy techniques and it was found that the MWCNTs were largely randomly dispersed in the PET matrix, but a small fraction were aligned in the extrusion flow direction due to the design of the die used in the extrusion process [11].

Table 1. Thermal properties of PET and composites of as extruded sheets of PET and MWCNTs, from DSC measurements [11].

Sample	T_g/°C	T_c/°C	T_m/°C	X_c/%
PET	84.5	194.1	254.1	28
PET1%	85.1	217.1	251.6	37
PET2%	84.9	220.1	251.8	35

Differential Scanning Calorimetry (DSC) measurements were performed on uniaxially deformed and annealed samples using a Mettler Toledo DSC822 instrument under a continuous flow of argon gas at 80 mL min^{-1}, calibrated with an indium metal standard. Samples of between 5 mg – 20 mg were loaded into standard 40 μL aluminium pans and heat-cool cycles were run from 30 °C to 270 °C at 10 °C min^{-1}. The percentage crystallinity X_c, of each sample was calculated using the following relationship:

$$X_c = \frac{\Delta H_f}{\Delta H_f^0 (1-\phi)} \quad (1)$$

where ΔH_f is the enthalpy of fusion from the integrated area under the melting transition from the DSC thermogram, ϕ is the weight fraction of MWCNTs blended with the PET homopolymer and ΔH_f^0 is the theoretical enthalpy change of 100% crystalline PET having a value of 117.6 J g^{-1}[32].

2.2 Instrumentation and synchrotron X-ray measurements.

Uniaxial deformation of the cast samples was performed using a purpose-built polymer film stretching instrument (Figure 1), which was positioned on beamline I22 of the Diamond Light Source, synchrotron, UK [33]. The X-ray energy used was 12.4 keV. The design and application of the stretching instrument with synchrotron radiation was previously reported by the authors [34,35]. The stretching instrument used was essentially an enclosed heated oven with two stepper motor driven pinions. Jaws attached to the pinions act as sample clamps. Samples of 5 mm width were secured to the clamps giving an initial gauge length (between the jaws) of 10 mm. Once clamped in place, the samples were located central to the beam position and drawn at a temperature of 110 °C with a draw ratio (DR) of 2.5:1 at rates of 0.1 s^{-1} and 0.2 s^{-1}. Load displacement data was recorded during the draw using a 500 N rated load cell located in one of the pinion shafts. Note only one jaw was programmed to move during the experiments. Post-drawn samples were then step annealed *in-situ* for 180 s at temperatures of 130, 160 and 190 °C.

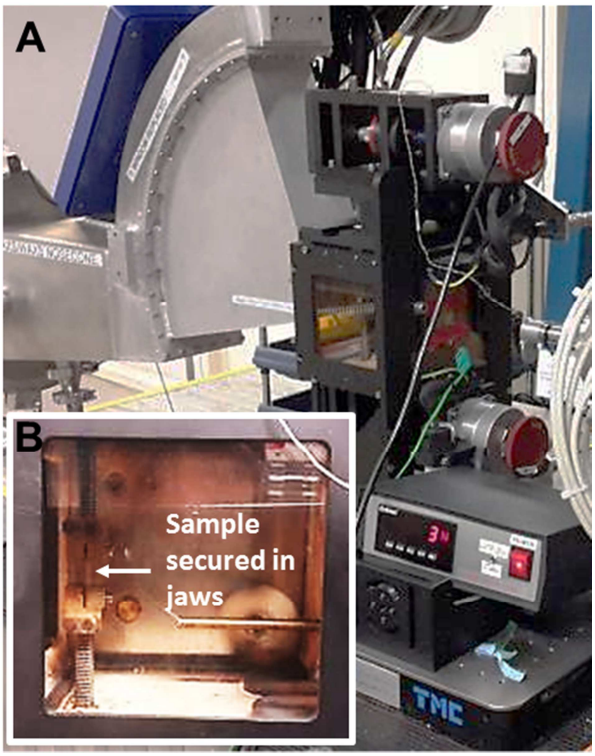

Figure 1. (A) Uniaxial stretching instrument on beamline I22. Inset (B) shows the sample secured in the clamps attached to the stepper motor pinions.

A vacuum chamber was positioned between the stretching instrument and SAXS detector reducing air scattering and absorption. SAXS data was recorded using a Pilatus P3-2M detector located at a distance of 5.38 m from the sample position and calibrated using silver behenate and oriented dry chicken collagen. During the drawing of the samples, SAXS data was taken at a frame rate of 200 ms. Subsequently, one frame of SAXS data was taken for 60 s at each annealing temperature. SAXS data frames of 60 s duration were also taken for the undrawn cast film at 30 °C and then at the same step annealing temperatures as the drawn film.

Two-dimensional WAXS data for the post-drawn and annealed samples were obtained on the XMaS (BM28) beamline [36] at the European Synchrotron Radiation Facility (ESRF), France with an X-ray beam energy of 12.0 keV. WAXS data was collected on a MAR-CCD detector at 20 s per frame, calibrated with silver behenate. The sample to detector distance was 340 mm.

2.3 SAXS/WAXS data analysis.

SAXS and WAXS data were normalized for sample thickness, transmission and background scattering. X-ray data reduction and analysis was performed using DAWN [37] and CCP13 Fibrefix [38] software suites. The 2D SAXS data was reduced to 1D scattering profiles of intensity (I) versus scattering vector (q), where $q = (4\pi/\lambda)\sin(\theta)$, 2θ is the scattering angle and λ is the X-ray wavelength. This was achieved by sector averaging symmetrically around the meridian (draw direction) by a fixed angle and radius, q. Radial azimuthal 1D profiles were also produced from the 2D SAXS data in order to estimate the relative orientation, where the angular variation in intensity, $I(q, \varphi)$, was obtained at a fixed radius q, over an azimuthal angle, φ, range of 0 - 360°. The two peaks in the 1D azimuthal profiles were then fitted using Gaussian functions to obtain the average full width half maximum (FWHM).

Correlation function analysis was performed on the 1D scattering profiles using a purpose-written correlation function program [39]. The correlation function, $\gamma(R)$, is expressed as:

$$\gamma(R) = \frac{1}{Q_s}\int_0^\infty I(q)q^2\cos(qR)\mathrm{d}q \qquad (2)$$

where $I(q)$ is the scattering intensity and Q_s is the experimental invariant obtained from the 1D SAXS profile scattering between the experimental limits of q_1 (the first real data point) and q_2 (the region where $I(q)$ is constant), expressed as:

$$Q_s(t) = \int_0^\infty q^2 I(q)\mathrm{d}q \approx \int_{q_1}^{q_2} q^2 I(q)\mathrm{d}q \qquad (3)$$

The correlation function was obtained from the extrapolation of SAXS data ($q \to \infty$) using a Porod [40] tail fit and linear back extrapolation ($q \to 0$). Several parameters were extracted from the correlation function which assumes an ideal two-phase lamellar morphology [41]; long

period, L_p, crystalline layer thickness L_c, amorphous layer thickness L_a and estimated bulk crystallinity X_c [42,43].

Stress-strain data analysis. For each drawing experiment, the load (N) and jaw displacement (mm) were recorded. From the load-displacement data, nominal stress-strain curves were obtained making the assumption that the cross-sectional area of the sample remained constant. This assumption is likely to be without error in the elastic region, but tends to be less reliable as plastic deformation occurs, although the relatively low draw ratio and lack of observed necking minimize errors. Strain at the beam position was estimated from the distance between the jaws. Elastic (Young's) modulus was determined from the initial linear portion of the stress-strain curve.

3 RESULTS AND DISCUSSION

3.1 Undrawn PET and PET-MWCNT composites: X-ray scattering data.

Static SAXS and WAXS patterns were taken of the extruded film before drawing to determine if any residual structure remained from the cast extrusion process. Figure 2, shows SAXS data for the undrawn cast film at room temperature then step annealed up to 190 °C. WAXS data for the cast film at 30 °C and post annealed at 190 ° C is given in the third and final columns respectively.

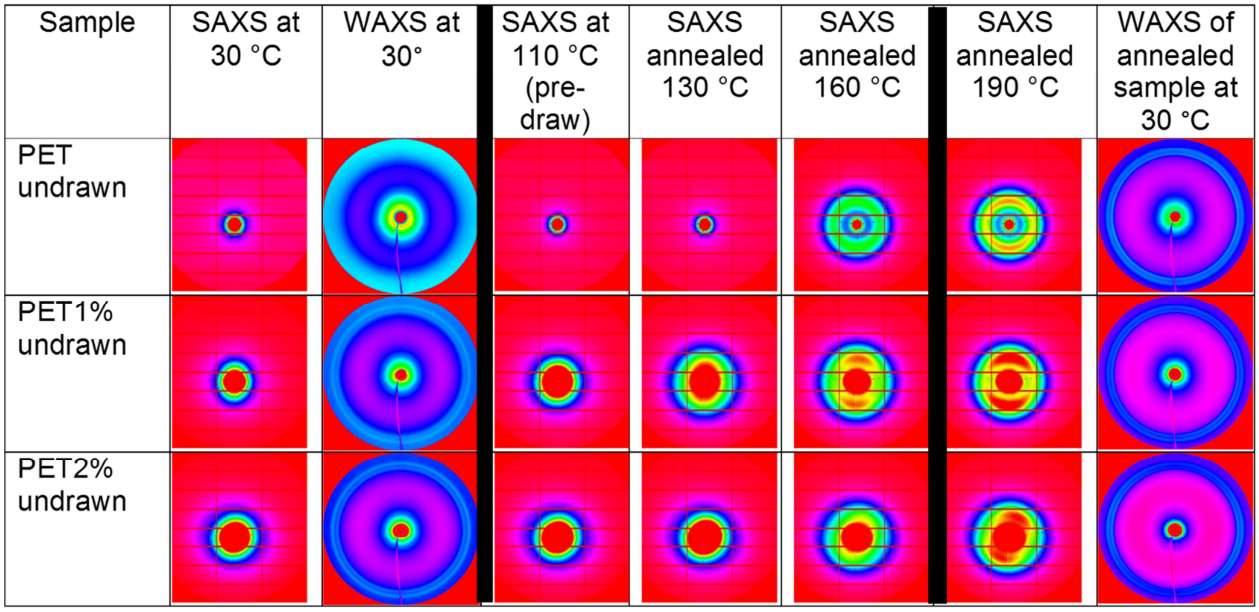

Figure 2. 2D SAXS/WAXS patterns for cast extruded PET and PET-MWCNT composite films during step annealing.

For the neat as cast extruded PET film at 30 °C, there is no obvious crystalline structure in either the SAXS or WAXS patterns induced by the processing method. In the WAXS data this is confirmed from the presence of a broad amorphous halo. As the sample is heated past T_g (85 °C) the SAXS shows a halo of intensity developing from 160 °C onwards. This is indicative of a largely randomly oriented lamellar crystalline structure, however some slight preferred orientation is observed owing to the increased intensity on the meridian (vertical direction). The PET WAXS pattern having been annealed at 190 °C, shows two sharp rings correlating to the $(0\bar{1}1)$ and (010) Bragg peaks of the PET triclinic unit cell [44].

In comparison, the PET-MWCNT composites show scattering in both the SAXS and WAXS patterns at 30 °C, indicated by the diffuse intensity around the central beamstop and clear $(0\bar{1}1)$ and (010) Bragg peaks, respectively. The SAXS scattering arises from both the MWCNTs and the crystalline PET component and as these samples are annealed the crystalline structure

continues to develop further. The SAXS shows some significant orientation of the crystalline structure, which is evident from the scattering arcs in the pattern. The WAXS shows some preferred orientation in the rings once annealed at 190 °C. A sharp WAXS peak corresponding to the ordered arrangement of MWCNTs usually seen at 2θ = 26.1° (as previously reported in Mayoral [11]). However this was not observed in the WAXS patterns in Figure 11, as this was beyond the experimental detector range.

The observed structure in the as cast extruded film is likely to be an outcome of the extrusion process, where for the PET-MWCNT composites, some oriented structure is locked in and does not relax during the casting process as the MWCNTs hinder polymer chain dynamics, compared to the neat PET. Similar residual structure has been seen in the extrusion of poly(ethylene) tapes, where increased draw down of the tape elongates the polymer chains which leads to a fibril or shish-kebab structure [45] rather than randomly oriented lamellae [46]. Hence, from the SAXS/WAXS patterns it is apparent that the MWCNTs have a significant influence on this residual orientation.

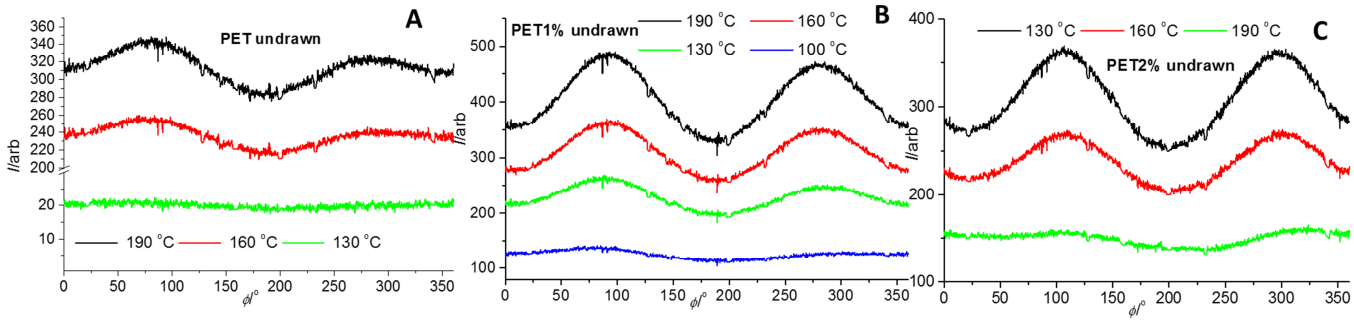

Figure 3. Azimuthal profiles from SAXS data of the undrawn step annealed (A) PET; (B) PET1% and (C) PET2% samples.

To investigate the relative orientation, azimuthal profiles were taken of the SAXS patterns which are shown in Figure 3, as the samples were annealed. The orientation in the PET and PET-

MWCNT composites increases with annealing temperature, indicated by the reduction in the width of the two peaks as they develop. A quantitative analysis of the peak widths was made by obtaining the average FWHM values where a fit was possible. Figure 4, shows the variation of FWHM with temperature for the undrawn samples.

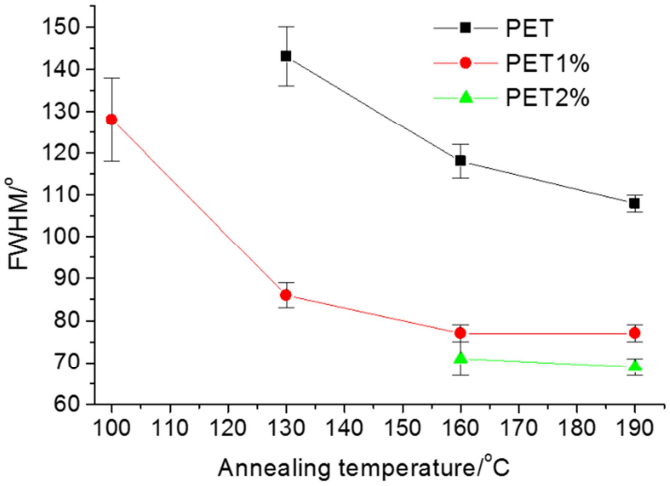

Figure 4. Change in FWHM for undrawn step annealed PET, PET1% and PET2% samples.

The relative orientation is seen to increase (FWHM decreases) in all samples with increasing annealing temperature. However, a large difference is seen on addition of MWCNTs to the PET. Both the PET1% and PET2% composites show increased orientation compared to neat PET which starts to level off at 160 °C. Whilst the azimuthal scans indicate some preferred orientation of the crystalline structure in the samples from the extrusion process, the arcing in the 2D SAXS patters indicates that there is still a range of orientations in these samples.

Correlation function analysis was performed on the 1D SAXS profiles obtained from the 2D SAXS patterns [39]. Figure 5A, shows 1D SAXS profiles of the undrawn annealed PET, PET1% and PET2% samples at 190 °C and Figure 5B, the corresponding correlation functions. Figure 5B also indicates the extracted parameters; long period L_p, crystalline layer thickness L_c,

amorphous layer thickness L_a and bulk crystallinity X_c from the correlation function. The extracted parameters are given in Table 2, for the undrawn annealed samples (note only data from 160 °C and 190 °C 1D SAXS profiles gave good correlation functions so extracted parameters could only be obtained from these fits with any reliability).

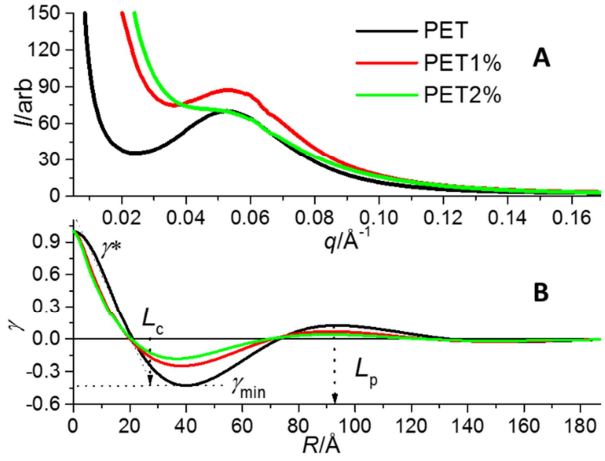

Figure 5. (A) 1D SAXS profiles for undrawn PET, PET1% and PET2% samples annealed at 190 °C and (B) corresponding correlation functions indicating extracted parameters: long period, L_p, crystalline layer thickness L_c, amorphous layer thickness L_a ($L_p - L_c$) and bulk crystallinity X_c (obtained from $\gamma_{min}/(\gamma_{min} - \gamma^*)$).

The data in Table 2, shows some small differences in the extracted correlation function parameters. The neat PET samples display the largest L_p and corresponding L_c values, but as the annealing temperature increases there is little change in these values. In comparison, the PET1% and PET2% samples have lower values of L_p and L_c at each annealing temperature, but L_p increases slightly with annealing temperature. However, the values of L_c remain relatively constant, whereas L_a, tends to increase. This indicates that some melting of the crystalline regions probably in the crystal-amorphous interface is occurring during annealing. One

significant difference observed is that both PET1% and PET2% show lower bulk crystallinity, PET2% being the lowest, compared to neat PET. Again this is mirrored in the reduced crystallite thicknesses in these blends.

Table 2. Extracted data from the correlation function analysis of the 1D SAXS profiles for PET, PET1% and PET2% undrawn step annealed samples.

Sample annealing temperature/°C	L_p/Å (± 4 Å)	L_c/Å (± 2 Å)	L_a/Å (± 2 Å)	X_c/% (± 2 %)
PET 160	93	27	66	25
PET 190	93	28	65	26
PET1% 160	88	21	67	18
PET1% 190	91	21	70	20
PET2% 160	86	19	67	14
PET2% 190	90	20	70	15

In this section we have detailed the structure development of the undrawn PET and PET-MWCNT composites during step annealing. The SAXS/WAXS data and subsequent analysis has shown that the cast extrusion process does induce some orientation and crystalline morphology in all the samples. The PET-MWCNT composites show greater crystalline orientation developing during annealing, but reduced crystallite size and bulk crystallinity compared to neat PET. Hence, initial conclusions are that the MWCNTs hinder the relaxation of the PET molecular chains during cast extrusion which later manifests as points for nucleation sites for crystalline lamellae growth. However, the MWCNTs can also hinder the extent that these crystalline regions grow and thicken, which is seen from the smaller crystallite thicknesses and overall lower bulk crystallinity in comparison to the neat PET. We now extend these analyses to

determine the effects MWCNTs have on the morphology development of PET under uniaxial deformation and subsequent annealing.

3.2 Uniaxially deformed PET and PET-MWCNT composites: mechanical properties. Stress-strain curves for the uniaxial deformation of PET, PET1% and PET2% for a DR of 2.5:1 at different rates are shown in Figure 6. Table 3, lists the elastic modulus values for the samples drawn at 110 °C with strain rates of 0.1 s^{-1} and 0.2 s^{-1}.

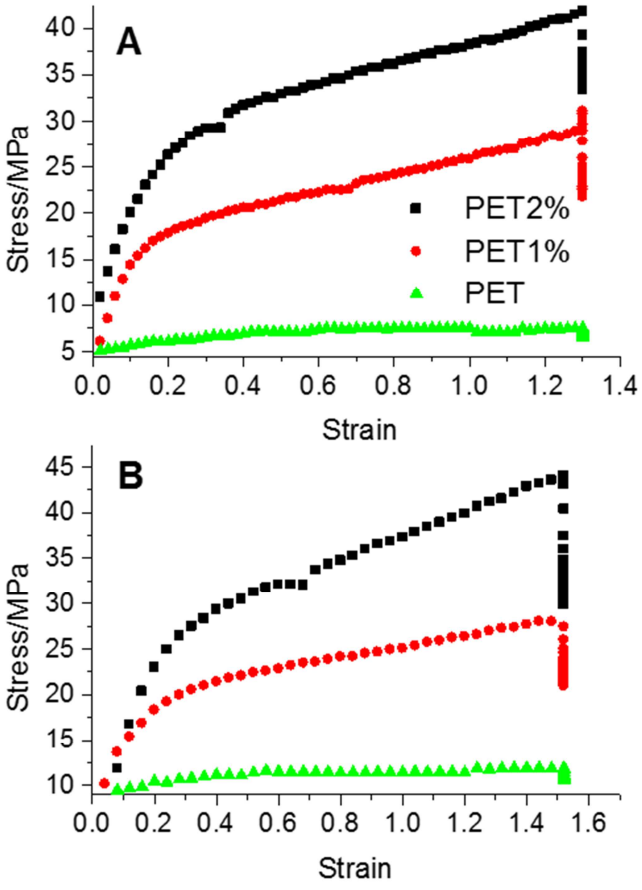

Figure 6. Stress-strain behavior during uniaxial deformation of PET, PET1% and PET2% at 110 °C; (A) DR 2.5:1 at 0.1 s^{-1}; (B) DR 2.5:1 at 0.2 s^{-1}.

All stress-strain curves show an elastic response initially followed by yield and strain hardening which progresses until the end of the draw [11,15]. Following the end of the draw, the sample relaxes as observed by the falling load at the maximum strain level attained.

Table 3. Elastic modulus of PET, PET1% and PET2% composite films uniaxially deformed at 110 °C.

Sample	Strain rate/s^{-1}	Young's modulus/MPa
PET	0.1	7
PET	0.2	7
PET1%	0.1	121
PET1%	0.2	87
PET2%	0.1	132
PET2%	0.2	110

The addition of MWCNTs to the PET significantly changed the mechanical properties, even at loadings as low as 1 wt%. From Figure 6, a dramatic increase in both the yield stress and the stress experienced at maximum strain was observed for the PET-MWCNT composites. This can be explained in two ways; supported by the data in in Table 1, and Figure 2, there is some residual crystalline morphology and orientation in the PET-MWCNT composites from the initial cast extrusion process which is not observed in the neat PET; furthermore the MWCNTs act as ties between the crystalline regions causing significant mechanical property changes. Modulus values rise from 7 MPa for the neat PET towards 100 MPa for the PET-MWCNT composites. It is interesting to note that the modulus of the PET-MWCNT composites may be strain-rate sensitive. At the higher strain-rate there is a drop in modulus which is somewhat counter-

intuitive. A possible explanation is that at the higher strain rate, there is increased load transfer to the weaker amorphous regions leading to an overall reduction in mechanical properties.

3.3 X-ray analysis of uniaxially deformed PET and PET-MWCNT composites.

2D SAXS data for the uniaxial deformation and annealing of the PET and PET-MWCNT composites were obtained to allow for a qualitative interpretation of the structure development to be made. SAXS patterns for polymers which have been subjected to shear deformation can be interpreted in terms of oriented lamellar or shish-kebab morphologies. Figure 7, shows some frequently observed SAXS patterns and their related morphologies [43,45-47]. These range from sharp spots for oriented lamellar type morphology to diffuse spots/arcs representing oriented shish-kebab morphology. The SAXS patterns and corresponding morphologies can be used interpret the developing morphology for the PET and PET-MWCNT composites, which are shown in Figure 8.

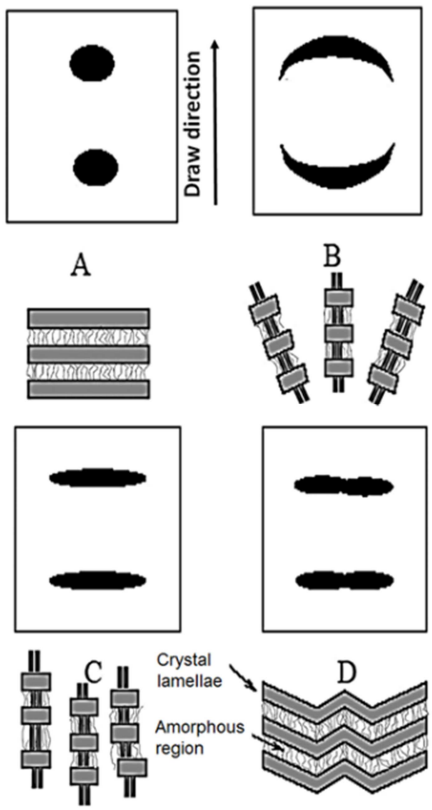

Figure 7. 2D SAXS patterns for oriented polymer samples. (A) Sharp meridional spots: broad parallel lamellae; (B) meridional arc: several orientations of narrow lamellae or shish-kebab structures; (c) diffuse spots: oriented fibrils with narrow lamellae or shish-kebab structures; (D) "four point" pattern: herringbone lamellar structure (adapted from Rober [45] and Heeley [46]).

The 2D SAXS patterns shown in Figure 8, include obvious differences in the morphology development of the neat PET compared to the PET-MWCNT composites during processing and annealing. The SAXS data post-draw at 110 °C and a strain rate of 0.1 s^{-1}, shows that the neat PET had very little initial structure, but as the sample is annealed a broad lamellar structure develops indicated by sharp meridional spots (Figure 7(A)). In contrast, both the PET1% and PET2% samples show significant diffuse post-draw scattering around the beamstop in the SAXS patterns.

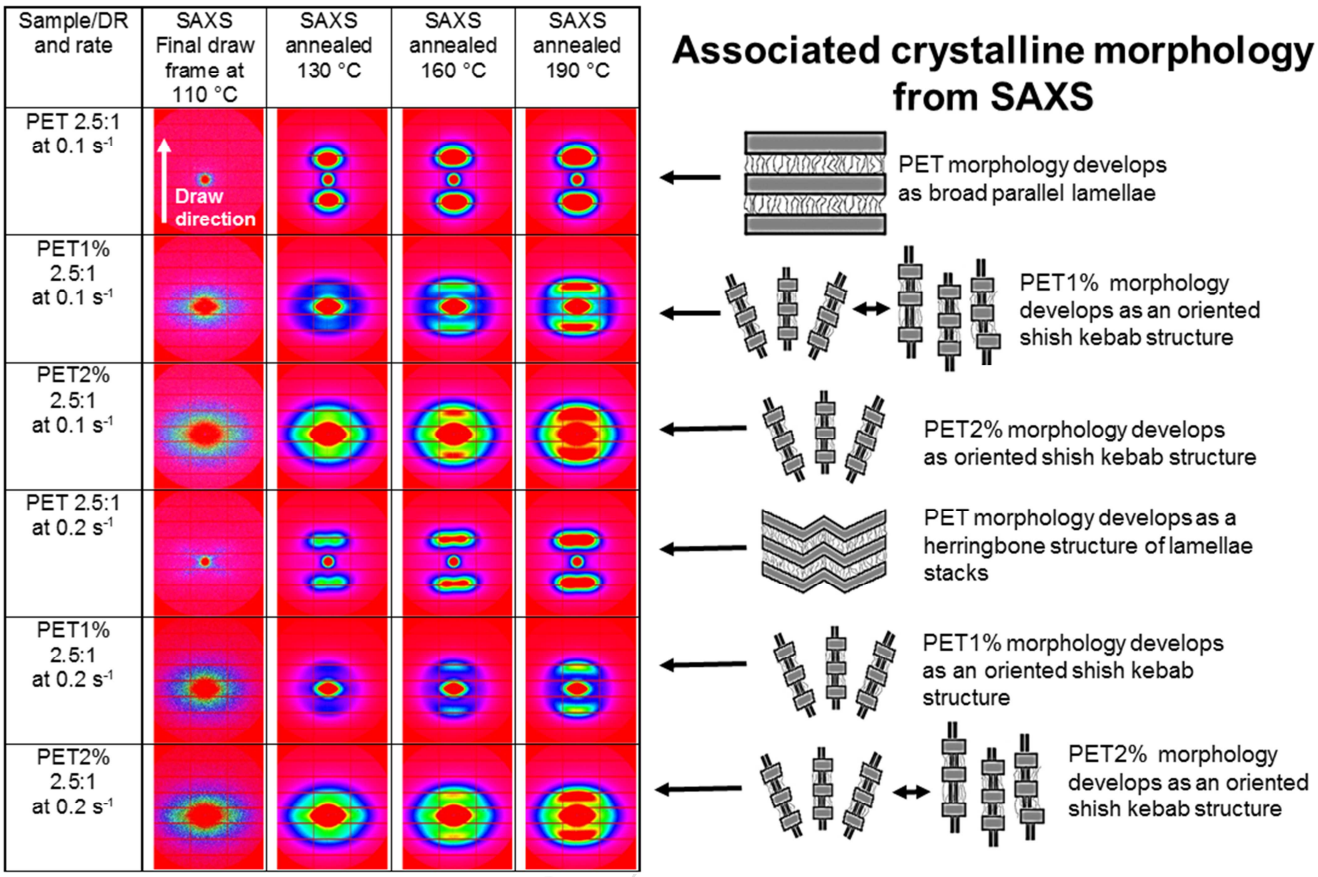

Figure 8. 2D SAXS patterns and associated morphology for the uniaxial deformation and subsequent step annealing of PET, PET1% and PET2%. Samples were drawn at a DR of 2.5:1 at a rate of 0.1 s^{-1} and 0.2 s^{-1}.

This is mostly likely due to the presence of the MWCNT filler (as it is clearly absent in the neat PET sample) and imperfect PET crystallites. As the PET-MWCNT samples are annealed, the SAXS data showed the development of meridional arcs and diffuse spots, which can be interpreted as narrow lamellae or shish-kebab structures with a variety of orientations around the vertical draw direction [43,46,47].

For the neat PET, as the draw rate increased to 0.2 s^{-1}, there is evidence of the initial formation of a 4-point pattern in the post-draw SAXS pattern at 110 °C. This is typically seen in the

development of the triclinic PET structure and its lamellae interpretation is that of a herringbone [48-50] or paracrystalline morphology [51] (Figure 7 (D)). The PET1% and PET2% composites again show a fibril or shish-kebab type of structure, but still significant diffuse scattering is observed in the SAXS patterns arising from the MWCNTs and imperfect PET crystallites.

Static 2D WAXS patterns of the drawn and annealed samples were taken at 30 °C and are shown in Figure 9. The neat PET sample shows the development of the triclinic PET structure, where the scattering reflections ($(0\bar{1}1)$ and (010)) are concentrated on the equator. This indicates the PET chains are oriented in the draw direction and the crystalline structure becomes more perfect with increasing draw rate (Figure 9 (A) and (B)), this is mirrored in the 2D SAXS.

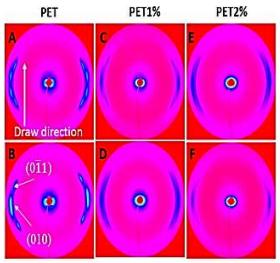

Figure 9. 2D WAXS patterns for uniaxially deformed (DR 2.5:1) step annealed samples of PET, PET1% and PET2%. (A) PET at 0.1 s^{-1}; (B) PET at 0.2 s^{-1}; (C) PET1% at 0.1 s^{-1}; (D) PET1% at 0.2 s^{-1}; (E) PET2% at 0.1 s^{-1}; (F) PET2% at 0.2 s^{-1}.

For the PET1% and PET2% composites, the 2D WAXS patterns again shows the triclinic crystal cell structure developing, but the $(0\bar{1}1)$ and (010) reflections tend to be arc-like rather than more spot-like as in the neat PET. This is again mirrored in the SAXS data were the shish-kebab crystalline structure is less oriented than the lamellar structure of PET. The comparative

amount of orientation in the samples can be obtained from the azimuthal profiles of the 2D SAXS patterns.

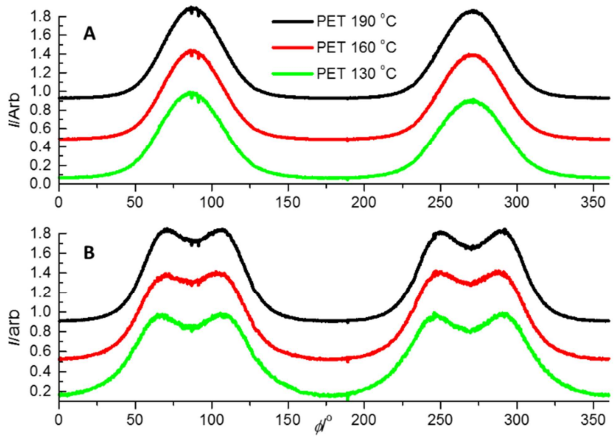

Figure 10. Azimuthal 1D SAXS profiles for PET post-draw (DR 2.5:1), during annealing at draw rates of (A) 0.1 s^{-1} and (B) 0.2 s^{-1}. (Scans offset in the vertical direction for clarity.)

Figure 10, shows the 1D azimuthal profiles for neat PET from the 2D SAXS patterns. The profiles clearly illustrate the change from a well oriented lamellar structure (Figure 10 (A)) to an oriented 4-point herringbone structure (Figure 10 (B)), as the draw rate was increased. It should also be noted that there is no discernable equatorial scattering in the profiles (φ angles 150° - 200°) for the neat PET. Similarly, the 1D azimuthal profiles for PET1% and PET2% composites are shown in Figure 11.

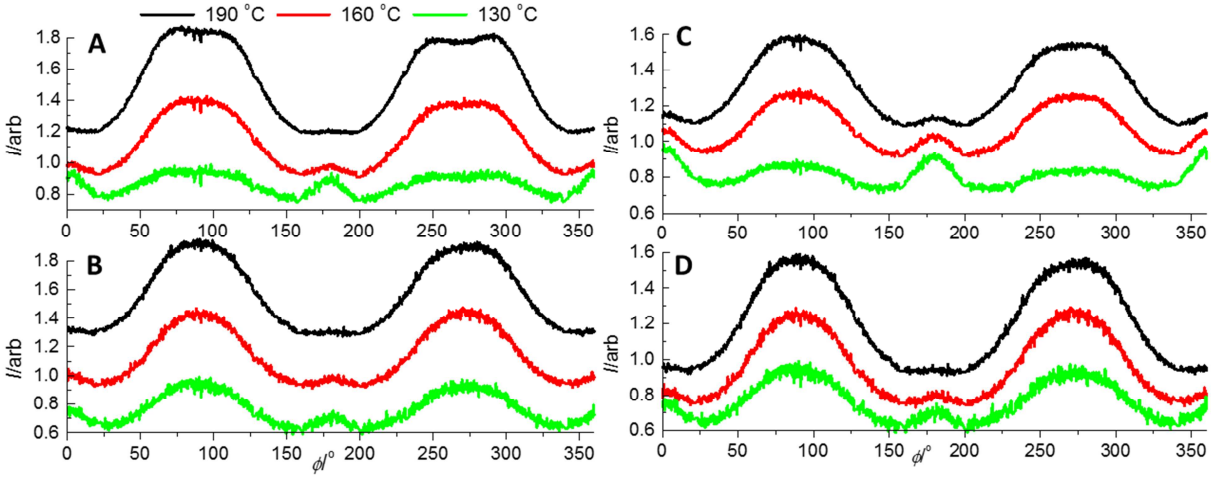

Figure 11. Azimuthal 1D SAXS profiles for PET1% and PET2% during annealing post-draw (DR 2.5:1). (A) PET1% at 0.1 s^{-1}; (B) PET1% at 0.2 s^{-1}; (C) PET2% at 0.1 s^{-1}; (D) PET2% at 0.2 s^{-1}. (Profiles offset in the vertical direction for clarity.)

The azimuthal profiles in Figure 11, for the PET1% and PET2% composites show broader peaks compared to neat PET (Figure 10). The profiles for PET1% (Figure 11 (A)) do show some evidence of the herringbone structure with the double peak but a 4-point pattern was not clearly defined in the 2D SAXS. With both the PET1% and PET2% composites there is distinct equatorial scattering seen at φ angles 150° - 200° which tends to diminish as the samples are annealed. This scattering can be attributed to the MWCNTs and imperfect PET crystalline and amorphous components. As the sample is annealed infill crystallization of more randomly oriented shish-kebab structures reduces the equatorial scattered intensity. The comparative change in orientation from the FWHM is shown in Figure 12, for all samples.

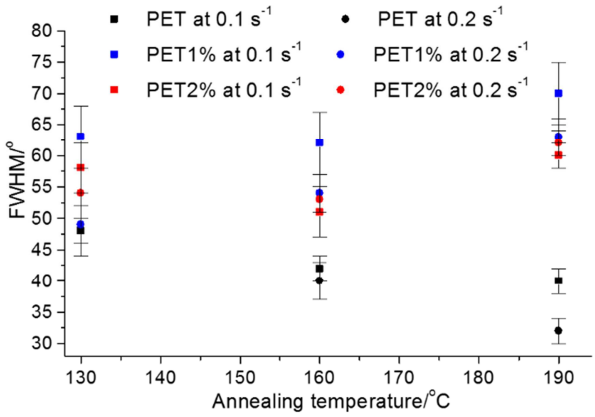

Figure 12. Change in orientation (FWHM) for PET and PET-MWCNT composites post-draw, at various annealing temperatures.

There is a significant difference in orientation between the neat PET and PET-MWCNT composites as the samples are step annealed. The neat PET sample has the greatest orientation over all annealing temperatures compared to the composites. The neat PET orientation increased (decrease in FWHM) as the annealing temperature increased. This is confirmed in both the 2D WAXS and SAXS patterns (Figures 8 and 9). Furthermore, for neat PET, the increase in draw rate also resulted in increased orientation, this is most apparent at the highest annealing temperature. This is not surprising as the higher stain rate would be expected to result in increased molecular orientation of the polymer chains in the draw direction [52].

The PET-MWCNT composites show an opposite effect with respect to orientation as annealing temperature was increased. The orientation does not change greatly when the samples were annealed up to 160 °C, but there is a reduction of orientation at the annealing temperature of 190 °C for both the PET1% and PET 2% composites. Here, the reduction in orientation can be explained by the crystallization of more shish-kebab structures but with greater variation in orientations, which would reduce the average overall orientation in the draw direction. This was observed also from the 2D SAXS data (Figure 8) where the meridional arcs become broader as

the annealing temperature was increased. From the data it can also be seen that increasing the draw rate has little effect on the orientation for the PET-MWCNT composites.

To determine the changes in long period, crystallite size and crystallinity with annealing temperature and draw rate, correlation functions were performed on the 1D SAXS profiles. The change in long period L_p, and crystalline region L_c, with annealing temperature and draw rate for all the samples are shown in Figure 13.

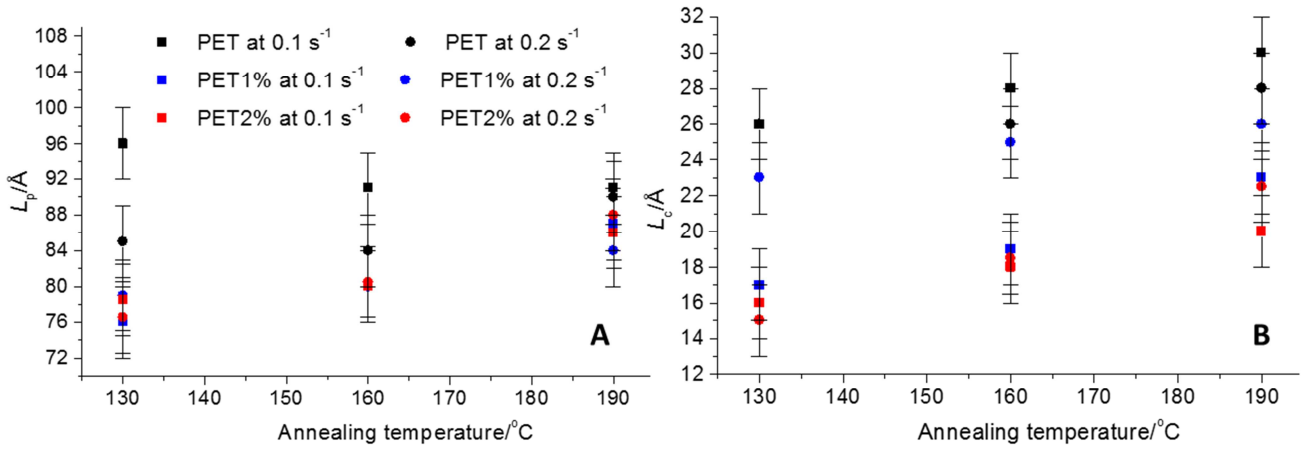

Figure 13. Change in (A) L_p and (B) L_c, for PET, PET1% and PET2% with annealing temperature for a DR of 2.5:1 and draw rates of 0.1 s^{-1} and 0.2 s^{-1}.

The L_p for the neat PET is greater than that for both PET1% and PET2% composites (Figure 13 (A)). Generally, L_p increases with annealing temperature is reflected in the increase in L_c (Figure 13 (B)), for all samples. However, the greatest increase in crystalline region is seen in the neat PET sample when annealed. The PET2% samples have the smallest L_c overall, regardless of annealing temperature and draw rate. The change in bulk crystallinity with increasing annealing temperature and draw rate for all samples is shown in Figure 14. Here, the data shows that the neat PET has the greatest bulk crystallinity and the PET2% shows the lowest crystallinity, although it should be noted that this behavior is strain-rate dependent [11].

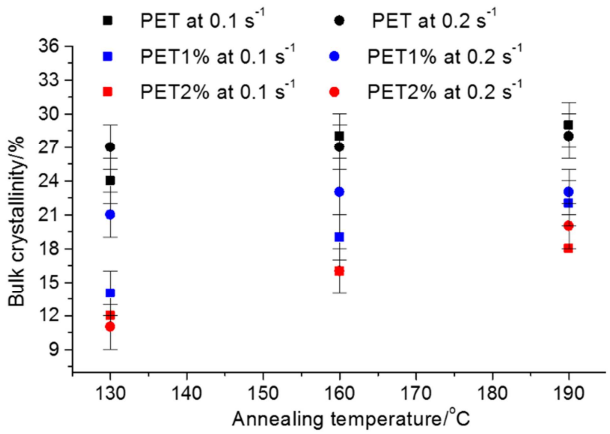

Figure 14. Change in bulk crystallinity, X_c, for PET, PET1% and PET2% samples with annealing temperature for a DR of 2.5:1 and draw rates of 0.1 s^{-1} and 0.2 s^{-1}.

The results from the correlation function analysis show that the addition of MWCNTs to PET can change the evolution of crystalline morphology significantly compared with the unfilled homopolymer. The crystalline regions and bulk crystallinity are reduced in the PET-MWCNT composites. Furthermore, from the FWHM analysis (Figure 12), the addition of MWCNTs to PET contributes to a reduction in chain orientation. This result supports that seen in the 2D SAXS/WAXS data. We see that the MWCNTs inhibit the development of a regular lamellar morphology (as is the case for neat PET), and instead a shish-kebab structure is formed. As the PET-MWCNT composites are annealed, new small crystallites are formed, but these can have more random orientations which is seen by the increase in the FWHM. However, the thermal behavior of PET and the PET-MWCNT composites (Table 1), suggests that the MWCNTs act as nucleating agents when the PET is crystallized – shown by a significant increase in T_c and X_c for the composites. To clarify the behavior described in this paper, thermal analysis was performed on drawn and annealed samples at 190 °C to investigate the T_c and crystallinity. The DSC heat-cool thermograms are shown in Figure 15.

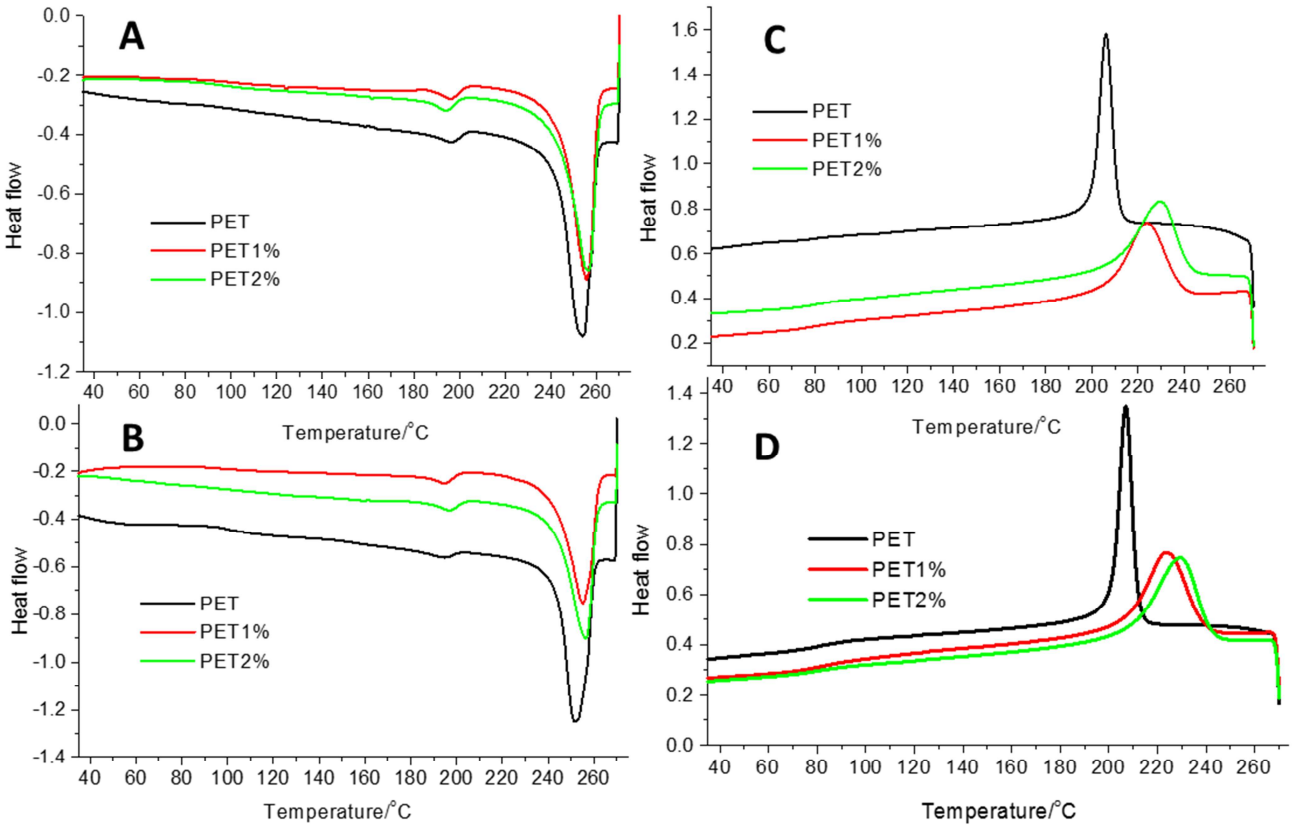

Figure 15. DSC heat-cool thermograms of post-drawn (DR 2.5:1) and annealed PET, PET1% and PET2% samples. (A) heat scan for samples at 0.1 s^{-1}; (B) heat scan for samples at 0.2 s^{-1}; (C) cool scan for samples at 0.1 s^{-1}; (D) cool scan for samples at 0.2 s^{-1}.

Both the melting and crystallization temperatures, and percentage crystallinity for these thermograms are collated in Table 4. The melting point of PET and PET-MWCNT composites does not change significantly and is similar to those values quoted in Table 1, for the as extruded cast films. The increased draw rate (0.1 s^{-1} to 0.2 s^{-1}) also has little effect on the melting temperature of PET. One interesting feature that is present in both the PET and PET-MWCNT composite heating thermograms is the small melting endotherm at ~196 °C. This 'double melting' peak of PET has been observed in uniaxially drawn and annealed PET films where the

lower temperature peak is attributed to the melting of imperfect small crystallites [53] and similarly in the PET-MWCNT composites [18,19].

Table 4. Thermal data for PET and PET-MWCNT composites post-draw and annealed at 190 °C.

Sample	T_c/°C		T_m/°C		X_c/%	
Draw rate/s^{-1}	0.1	0.2	0.1	0.2	0.1	0.2
PET	207.3	206.4	253.6	251.8	43	39
PET1%	224.1	224.0	255.3	254.8	41	38
PET2%	229.7	230.0	256.1	256.0	37	35

From Table 4, it can be seen that there is a considerable increase in the crystallization temperature T_c, for the PET-MWCNT composites compared with the neat PET. This is expected assuming the MWCNTs act as nucleating agents as was shown earlier for the thermal analysis of the as extruded cast materials (Table 1). The crystallinity for the neat PET is greater than that for the PET-MWCNT composites which is in contrast to the crystallinity of the as cast extruded samples. The crystallinity is reduced in all samples with increasing draw rate. Thus, although the MWCNTs in the drawn samples still nucleate crystal growth heterogeneously (i.e. crystallization kinetics are increased) the final bulk crystalline component is reduced in comparison to neat PET. This was also seen from the correlation function analysis where the crystallite size was reduced and therefore the overall crystallinity. This is further confirmed from the 2D SAXS showing the formation of a shish-kebab morphology rather than lamellar structure for neat PET. The broadening of the crystallization peaks in the cooling thermograms for the PET-MWCNT

composite samples (Figure 5C and 5D), is again attributed to a range of imperfect crystallites formed via heterogeneous nucleation.

From the results presented here for both the as cast extruded and uniaxially deformed samples, it can be seen that MWCNTs do act as nucleating agents, increasing crystallization kinetics. However, significant differences are seen in the evolution of the crystalline morphology during uniaxial deformation. The PET-MWCNT composites have a prevalent shish-kebab structure, where the MWCNTs inhibit crystallite growth and reduce the overall crystalline orientation. Conversely, a regular well developed lamellar structure with significant orientation is seen for the unfilled PET homopolymer under the same processing conditions.

The differences in PET morphology are undoubtedly due to the addition of MWCNTs. From the published literature it has been argued [25-28] that CNTs act as the shish so that the PET crystallites (kebabs) then grow expitaxially from these shish, thus the CNTs act as nucleating points in this process. Therefore, the nanohybrid shish-kebab structure (NHSK) [25-30] proposed for PE and iPP CNT composites is valid here with respect to our PET-MWCNT composites. However, the MWCNTs tend to hinder PET chain orientation during deformation, which leads to a more random orientation in the emerging crystallites, thus a reduction in orientation as crystallization progresses. The MWCNTs also obstruct the thickening of the crystallites into a full lamellar structure, like that described for the PET homopolymer. Therefore, it is probable that some crystallites are initially nucleated by the MWCNTs acting as shish but as the annealing temperature is increased, crystallites in the PET matrix also nucleate and grow. This scenario would imply that PET crystallites result from both nucleation in the PET matrix and at the surface of the MWCNTs [31].

The NHSK or MWCNT/matrix nucleation and subsequent crystal growth models for PET-MWCNT composites are both credible mechanisms, but it is difficult to separate these crystallization mechanisms even with the data presented here. As a result, the NHSK model combined with polymer matrix nucleation and crystal grown mechanism provides an overall plausible description of the crystallization mechanism observed here with PET-MWCNT composites during uniaxial deformation at low strain rates.

4 CONCLUSIONS

Combined SAXS/WAXS, mechanical and thermal techniques have been employed to follow the morphology evolution in a set of PET-MWCNT composites as cast extruded films and during solid-state uniaxial deformation and subsequent annealing. The results revealed that following cast extrusion, the PET-MWCNT films retained residual orientation and had increased crystallinity due to the processing equipment used (related to the land length of the die used during extrusion), whereas the neat PET did not. The PET-MWCNT composites once uniaxially deformed at a DR of 2.5:1 at low strain rates, showed significantly improved mechanical properties and a different crystalline morphology compared with neat unfilled PET. SAXS data revealed a regular well developed lamellar structure with significant orientation for neat PET, conversely the PET-MWCNT composites showed a shish-kebab morphology with reduced orientation. The MWCNTs in the polymer composite increase nucleation events, but inhibit the growth of crystallite structure and reduce the overall crystalline orientation. Once annealed, the final crystallite thickness and bulk crystallinity is reduced in the composite samples. WAXS data confirmed the orientation to be greater in the neat PET, but no change in the crystallite PET unit cell was observed due to the addition of MWCNTs. Moreover, thermal analysis of the drawn and

annealed films showed that the MWCNTs act as nucleating agents, increasing the rate of crystallization, but the final crystalline content in the composites is actually less than that for neat PET.

The data has shown the definitive role MWCNTs have in the structural evolution in PET during uniaxial deformation. Whilst the MWCNTs act as nucleating agents (increasing crystallization kinetics), they form a shish-kebab morphology compared to the well-developed lamellar structure seen for neat PET. The mechanism of the formation of this morphology is attributed to the MWCNTs acting as shish for the epitaxial PET crystallites to grow out from, that is, a nanohybrid shish-kebab structure (NHSK) is formed. Furthermore, nucleation and crystal growth also occurs in the PET matrix, but the MWCNTs inhibit crystallite development and hinder any perfection to a full lamellar structure.

The results here have provided a valuable insight into the role of MWCNTs as a functional nanofiller for polymers. The improved mechanical properties can be linked to the MWCNTs reinforcement and nucleating effects and thus the crystalline structure development when processed. However, contrary to this MWCNTs then inhibit crystal growth of the polymer when further processing occurs, reducing overall bulk crystallinity and orientation, in comparison with the homopolymer itself. This could have wide-spread application in modifying polymers with MWCNTs where the structure and physical properties can be tailored to function.

ACKNOWLEDGMENT

X-ray beam time at Diamond Light Source was provided under the experimental application SM-11742. ESRF beamtime was provided under the experimental application 28-01/1127. We are grateful for the assistance of all the Diamond I22 and ESRF BM28 (XMaS) beamline staff.

REFERENCES

[1] Grady, B. P. *Carbon nanotube-polymer composites manufacture, properties, and applications*, 1st Ed. Wiley-Interscience: New York, 2011.

[2] Feldman, D. J. Macromol. Sci. A, **2015**, *52*, 648-658.

[3] Spitalsky, Z.; Tasis, D.; Papagelis, K.; Galiotis, C. *Progress in polymer science*, **2010,** *35*, 357-401.

[4] Breuer, O.; Sundararaj, U. *Polymer composites* **2004**, *25*, 630-645.

[5] Xie, X. L.; Mai, Y. W.; Zhou, X. P. *Materials Science and Engineering: R: Reports*, **2005,** *49*, 89-112.

[6] Coleman, J. N.; Khan, U.; Blau, W. J.; Gun'ko, Y. K. *Carbon*, **2006**, *44*, 1624-1652.

[7] McNally, T.; Pötschke, P. *Polymer-carbon nanotube composites: Preparation, properties and application*, Cambridge United Kingdom: Woodhead Publishing, 2011.

[8] Pandey, G.; Thostenson, E. T. *Polymer Reviews*, **2012**, *52*, 355-416.

[9] Wernik, J. M.; Meguid, S. A. *Appl. Mech. Rev.*, **2010**, *63*, 050801-050801-40.

[10] Kim, J. Y.; Kim. S. H. In *High Performance PET/Carbon Nanotube Nanocomposites: Preparation, Characterization, Properties and Applications, Nanocomposites - New Trends and Developments*, Ebrahimi, F., Ed.; InTech, 2012, Chap. 5. DOI: 10.5772/50413.

[11] Mayoral, B.; Hornsby, P. R.; McNally, T.; Schiller, T.L.; Jack, K.; Martin D.J. *RSC Adv*. **2013**, *3*, 5162-5183.

[12] McCrossan, K.; McClory, C.; Mayoral, B.; Thompson, D.; McNally, T.; Murphy, M.; Nicholson, T.; Martin, D.; Halley, P. (2011). In *Composites of poly(ethylene terephthlate) and carbon nanotubes. Polymer-carbon nanotube composites: Preparation, properties and application*, McNally, T.; Pötschke, P; Eds, Cambridge United Kingdom: Woodhead Publishing, 2011; p 545.

[13] Cruz-Delgado, V.J.; Ávila-Orta, C. A.; Espinoza-Martínez, A. B.; Mata-Padilla, J. M.; Solis-Rosales, S. G.;. Jalbout, A. F; Medellín-Rodríguez, F. J.; Hsiao. B. S. *Polymer*, **2014**, *55*, 642-650.

[14] Antoniadis, G.; Paraskevopoulos, K. M.; Bikiaris, D.; Chrissafis, K. *J. Polym. Sci. B Polym. Phys.*, **2009**. *47*, 1452-1466.

[15] Mazinani,S.; Ajji, A.; Dubois, C. *Polym. Eng. Sci*. **2010**, *50*, 1956-1968.

[16] Zaman, H. U.; Hun, P. D.; A. Khan, R. A., Yoon, K-B. *Fullerenes, Nanotubes and Carbon Nanostructures*, **2013**, *21*, 701-711.

[17] Kim, J. Y.; Park, H. S.; Kim, S. H. *J. Appl. Polym. Sci.*, **2007**, *103*, 1450–1457.

[18] Tzavalas, S.; Mouzakis, D. E.; Drakonakis, V.; Gregoriou, V. G. *J. Polym. Sci. B Polym. Phys.* **2008**, *46*, 668-676.

[19] Tzavalas, S.; Drakonakis, V.; Mouzakis, D.E.; Fischer, D.; Gregoriou, V. G. *Macromols*, **2006**, *39*, 9150-9156.

[20] Anand, K. A.; Agarwal, U. S.; Joseph, R. *Polymer*, **2006**, *47*, 3976-3980.

[21] Vad, T.; Wulfhorst, J.; Pan, T-T.; Steinmann, W.; Dabringhaus, S.; Beckers, M.; Seide, G.; Gries, T.; Sager, W. F. C.; Heidelmann, M.; Weirich. T. E. *Macromols*, **2013**, *46*, 5604-5613.

[22] Hur, J. W.; Yoo, H. J.; Cho, J. W.; Kim, K. H. J. *Polym. Sci. Part B: Polym. Phys*., **2015**, DOI: 10.1002/polb.23953.

[23] Chen, H.; Liu, Z.; Cebe, P. *Polymer*, **2009**, *50*, 872-880.

[24] Deng, H.; Bilotti, E.; Zhang, R.; Peijs, T. *J. Appl. Polym. Sci.*, **2010**, *118*, 30-41.

[25] Laird, E. D.; Li, C. Y. *Macromols*, **2013**, *46*, 2877-2891.

[26] Li, C. Y., Li, L., Cai, W., Kodjie, S. L. and Tenneti, K. K. *Adv. Mater.*, **2005**, *17*, 1198-1202.

[27] Li, L.; Li, B.; Hood, M. A.; Li. C. Y. *Polymer*, **2009**, *50*, 953-965.

[28] Patil, P.; Balzano, L.; Portale, G.; Rastogi, S. *Carbon*, **2010**, *48*, 4116-4128.

[29] Liu, P.; White, K. L.; Sugiyama, H.; Xi, J.; Higuchi, T.; Hoshino, T.; Ishige, R.; Jinnai, H.; Takahara, A.; Sue, H.J.; 2013.. *Macromols*, **2013**, *46*, 463-473.

[30] Chen, Y. H.; Zhong, G. J.; Lei, J.; Li, Z. M.; Hsiao, B. S. *Macromols*, **2011**, *44*, 8080-8092.

[31] Wurm, A.; Lellinger, D.; Minakov, A. A.; Skipa, T.; Pötschke, P.; Nicula, R.; Alig, I.; Schick, C. *Polymer*, **2014**, *55*, 2220-2232.

[32] Metha, A.; Gaur, U.; Wunderlich, B. J. *Polym. Sci., Polym.Phys. Ed.*, **1978**, *16*, 289-296.

[33] I22: Small Angle Scattering & Diffraction. http://www.diamond.ac.uk/Beamlines/Soft-Condensed-Matter/small-angle/I22.html (*Assessed 15/03/2016*)

[34] Hughes, D. J.; Mahendrasingam, A.; Oatway, W. B.; Heeley, E. L., Martin, C.; Fuller, W. *Polymer*, **1997**, *38*, 26, 6427-6430.

[35] Hughes. D. J.; Mahendrasingam, A.; Martin, C.; Oatway, W.B.; Heeley, E.L.; Bingham, S. J.; Fuller, *W. Rev. Sci. Instrum.*, **1999**, *70*, 4051-4054.

[36] XMaS: The UK Materials Science Facility at the ESRF. http://www2.warwick.ac.uk/fac/cross_fac/xmas/ (*Assessed 15/03/2016*)

[37] Basham, M.; Filik, J.; Wharmby, M. T.; Chang, P. C. Y.; El Kassaby, B.; Gerring, M.; Aishima, J.; Levik, K.; Pulford, B. C. A.; Sikharulidze, I.; Sneddon, D.; Webber, M.; Dhesi, S. S.; Maccherozzi, F.; Svensson, O.; Brockhauser, S.; Náray, G,; Ashton, A. W. *J. Synchrotron Rad.*, **2015**, *22*, 853-858.

[38] FibreFix. http://www.diamond.ac.uk/Beamlines/Soft-Condensed-Matter/small-angle/SAXS-Software/CCP13/FibreFix.html (*Assessed 15/03/2016*)

[39] Simple SAXS and WAXS Software written in Excel. http://coecs.ou.edu/Brian.P.Grady/saxssoftware.html#Allprograms (*Assessed 15/03/2016*)

[40] Porod G, *Kolloid Z*, **1951**, *124*, 83-114.

[41] Baltá-Calleja, F.J,; Vonk ,G. G. *X-ray scattering of synthetic polymers*. Elsevier Science, New York, **1989**.

[42] Ryan, A. J. *Fibre Diffr. Rev*. **1994**, *3*, 25-29.

[43] Heeley, E. L.; Gough, T.; Hughes, D. J.; Bras, W.; Rieger, J. and Ryan, A. J. *Polymer*, **2013**, *54*, 6580-6588.

[44] Daubeny, R. de P,; Bunn, C. W. *Proc. R. Soc. Lond. A*, **1954**, *226*, 531-542.

[45] Rober, S,; Bosecke, P,; Zachmann, H. G. *Makromol. Chem. Macromol. Symp.*, **1988**, *15*, 295-310.

[46] Heeley, E. L.; Fernyhough, C. M.; Graham, R. S.; Olmsted, P. D.; Inkson, N. J.; Embery, J.; Groves, D. J.; McLeish, T. C. B.; Morgovan, A. C.; Meneau, F.; Bras, W.; Ryan, A. J. *Macromols*., **2006**, *39*, 5058-5071.

[47] Abou-Kandil, A, I.; Windle. A. H. *Polymer*, **2007**, *48*, 5069-5079.

[48] Mahendrasingam, A.; Blundell, D. J.; Wright, A. K.; Urban, V.; Narayanan, T.; Fuller, W. *Polymer*, **2003**, *44*, 5915-5925.

[49] Uchiyama, T.; Suyama, M.; Alam, M. M.; Asano, T.; Henning, S.; Flores, A.; Baltá Calleja, F. J.; Mina. M.F. *Polymer*, **2007**, *48*, 542-555.

[50] Asano, T.; Baltá Calleja, F. J.; Flores, A.; Tanigaki, M.; Mina, M. F.; Sawatari, C.; Itagaki, H.; Takahashi, H.; Hatta. I. *Polymer*, **1999**, *40*, 6475-6484.

[51] Rule, R. J.; MacKerron, D. H.; Mahendrasingam, A.; Martin, C.; Nye. T. M. W. *Macromols*., **1995**, *28*, 8517-8522.

[52] Blundell, D. J.; Mahendrasingam, A.; Martia, C.; Fuller, W.; MacKerron, D. H.; Harvie, J. L.; Oldman, R. J.; Riekel. C. *Polymer*, **2000**, *41*, 7793-7802.

[53] Tongyin, Y.; Haishan, B.; Jiacong, H.; Wei, Z.; Qiaoying, G. *Polymer communications*, **1983**, *1*, 83-91.

Highlights

1. Morphology evolution and crystallinity of PET-MWCNT composite films was investigated.

2. Uniaxially deformed PET-MWCNT films displayed improved mechanical properties.

3. SAXS/WAXS data revealed a well oriented lamellar structure for unfilled PET films.

4. PET-MWCNT composites revealed a nanohybrid shish-kebab (NHSK) morphology.

5. The MWCNTs act as shish for the epitaxial growth of PET crystallites (kebabs).